Energy 292 (2024) 130490

Contents lists available at ScienceDirect

Energy

journal homepage: www.elsevier.com/locate/energy

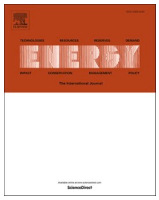

Thermo-hydro-chemical modeling and analysis of methane extraction from fractured gas hydrate-bearing sediments

Ming Yang [a], Yuze Wang [a,*], Hui Wu [b,c,**], Pengwei Zhang [d], Xin Ju [e]

[a] Department of Ocean Science and Engineering, Southern University of Science and Technology, Shenzhen, Guangdong 518055, China
[b] School of Earth and Space Sciences, Peking University, Beijing 100871, China
[c] Peking University Ordos Research Institute of Energy, Ordos, 017010, China
[d] Key Laboratory of Urban Underground Engineering of Ministry of Education, Beijing Jiaotong University, Beijing 100044, China
[e] Department of Energy Science and Engineering, Stanford University, Stanford, CA 94305, USA

ARTICLE INFO

Handling Editor: Wojciech Stanek

Keywords:
Methane hydrate dissociation
Thermo-hydro-chemical relationship
Gas production enhancement
Fracture
Dimensional analysis
Numerical simulation

ABSTRACT

Hydraulic fracturing is widely used in enhancing hydrocarbon recovery efficiency of unconventional reservoirs including gas hydrate-bearing sediment (GHBS). However, the underlying mechanisms governing the influences of fractures on the intricate multi-field coupled processes during methane extraction remain poorly understood. This study develops a fully coupled thermo-hydro-chemical (THC) model for methane extraction from fractured GHBS under combined heat injection and depressurization operations. Novel dimensionless numbers are proposed to characterize the underlying heat transfer, fluid flow, and hydrate decomposition processes. The results reveal that depressurization induced fluid flow dominates methane extraction in the early stages, while heat injection induced thermal processes become the primary controlling factor in the intermediate and long-term stages. The flow field primarily governs the global-scale hydrate decomposition process, whereas the thermal field dictates the local-scale evolution of the pre-decomposition front. We find that increasing injection temperature and decreasing production pressure could improve gas recovery efficiency, although economic consideration may constrain these production strategies. Particularly, increasing injection temperature expands local hydrate decomposition zone and boosts gas production, while depressurization at the production well reduces the overall gas hydrate saturation and leads to extra gas production. Variation in well spacing show little effect on the gas recovery efficiency, but the total gas production changes for the change of reservoir scale. This study provides insights into the mechanisms of coupled thermo-hydro-chemical behaviors during methane extraction from fractured GHBS, and offers a fundamental model for the optimization of both extraction efficiency and economic viability of gas hydrate recovery.

1. Introduction

In recent years, the growing global demand for renewable energy has led to intense interests in natural gas hydrates (NGH) as an emerging clean energy source. NGH, also known colloquially as combustible ice, is a crystalline compound consisting of light hydrocarbon molecules [1]. NGH deposits are typically found in high-pressure, low-temperature environments such as marine sediments and permafrost regions [1]. According to Milkov's 2004 study, the ocean contains approximately 2.5×10^{15} m^3 of NGH resources, demonstrating a significant opportunity for development [2]. As such, countries worldwide are actively engaged in the research of NGH exploration and development, employing various conventional extraction methods, including depressurization [3–7], thermal stimulation [8–11], inhibitor injection [12,13], and carbon dioxide displacement [14], etc.

Although several successful field trials have been conducted using these methods, methane extraction efficiency remains limited due to low productivity, short stable production time, and narrow hydrate spatial decomposition region during on-site tests [15]. The low permeability of gas hydrate-bearing sediment (GHBS) is the major issue that prevents commercially efficient methane extraction [16]. Anderson et al. estimated the GHBS permeability of Mount Elbert area in the United States by matching historical data, and the result was between 0.12 and 0.17 mD [17]. Dai et al. measured the permeability of in-situ core samples from GHBS in the Indian Ocean, which was only 0.04 mD [18]. Jiang

* Corresponding author.
** Corresponding author. School of Earth and Space Sciences, Peking University, Beijing 100871, China.
E-mail addresses: wangyz@sustech.edu.cn (Y. Wang), hui.wu@pku.edu.cn (H. Wu).

https://doi.org/10.1016/j.energy.2024.130490
Received 19 July 2023; Received in revised form 4 December 2023; Accepted 25 January 2024
Available online 30 January 2024

Nomenclature

C	Mass heat capacity (J/(kg·K))
Da	Damköhler number (−)
E	Specific internal energy (J/kg)
$\boldsymbol{g}$	Gravity vector $(0, 0, -9.81 \mathrm{m/s^2})$
H	Specific enthalpy (J/kg)
k_0	Intrinsic permeability ($\mathrm{m^2}$)
k_r	Relative permeability (−)
K_b	Klinkenberg factor
λ	Thermal conductivity (W/(m·K))
μ	Viscosity of fluid (Pa·s)
L	well spacing (m)
M	Molecule weight (g/mol)
P	Pressure (Pa)
φ	Porosity (−)
q	Mass source and sink ($\mathrm{kg/(s \cdot m^3)}$)
R	Dynamic dimensionless number (−)
ρ	Density ($\mathrm{kg/m^3}$)
S	Phase saturation (−)
t	Time (s)
T	Temperature (K)
τ	Characteristic time (−)
v	Velocity of fluid (m/s)

Subscripts

a	Aqueous phase
g	Gaseous phase
h	Hydrate phase
c	Capillary
s	Sediment matrix
r	Parameters in reference state
0	Original or initial state
f	Fracture
inj	Injection well
prod	Production well

Abbreviations

NGH	Natural gas hydrate
GHBS	Gas hydrate-bearing sediment
HFZ	Hydrate-free zone
BGZ	Background zone
STP	Standard temperature and pressure

et al. performed permeability tests on hydrate core samples from the Ulleung Basin, Korea, and the result was as low as 0.01 mD [19]. In China's second hydrate reservoir trial production of Shenhu area, South China Sea, scientists found that the GHBS permeability was 2.38 mD [3]. In comparison, conventional oil and gas reservoirs typically exhibit permeability values of 100 mD or greater. To overcome the low permeability challenge, various methods have been proposed to enhance reservoir permeability, and thus improve methane production efficiency. For example, Liu et al. investigated hydraulic fracturing as a production enhancement technology for NGH through numerical simulations and model experiments, and the results verified the effectiveness of hydraulic fracturing in enhancing gas production [20]. However, Sun et al. found that hydraulic fracturing alone was insufficient to ensure long-term efficient gas production from fine-grained reservoirs [21]. Combining hydraulic fracturing with depressurization has proven an effective method to increase gas production, especially with optimized fracturing and depressurization parameters [22–27]. Additionally, researchers have proposed various approaches to addressing issues such as excessive water production during hydrate extraction, including combining hydraulic slotting and burden sealing methods [28,29] as well as physical and chemical methods for reservoir re-heating [30–32].

The extraction of methane from GHBS entails intricate physical and chemical mechanisms, such as fluid flow in fractures and matrix, heat transfer, and hydrate decomposition. These processes play different roles at different stages. Some researchers also performed preliminary mechanistic analysis into synergistic hydrate extraction methods with the purpose of developing more efficient techniques to enhance gas production from GHBS. Feng et al. conducted hydrate dissociation experiments using large-scale simulator and presented that balancing the depressurizing rate and heat transfer rate is crucial for enhancing gas production [33]. Ju et al. proposed a method combining depressurization, hot water injection, and hydraulic fracturing. Their results indicated that thermal breakthrough was a critical signal of hydrate production mode [34]. Sun et al. performed laboratory experiments and found that hydraulic fracturing could significantly increase gas production in early stages, but its effectiveness was limited in later stages [21]. Ning et al. verified such a reduced effectiveness through numerical simulation and indicated that load sealing could improve long-term gas production efficiency [29]. Yu et al. have revealed that fractures with different orientations exhibit divergent impacts across varying time scales, whereby vertical fractures enhance short-term gas production efficiency while horizontal fractures primarily affect long-term gas production behavior [35]. Oluwunmi et al. conducted simulations of geological cycles spanning over 8000 years and observed that the evolution of the flow field progressed significantly faster than the variation of the temperature field. This suggests that the temperature field plays a crucial role in maintaining the long-term stability of sedimentary hydrates [36]. Li et al. conducted indoor experiments on methane hydrate formation and decomposition with different porous medium conditions. They found that fluid flow and heat transfer played different roles in hydrate formation and decomposition [37]. Teng et al. performed dimensional analysis and proposed several dimensionless numbers to clarify the relationship between hydrate decomposition kinetics and fluid flow field under various spatial scales (reactor scale and reservoir scale) [38]. Previous studies also proposed several dimensionless models to describe the relation between fluid flow and hydrate reaction [39,40]. However, there are no dimensionless analytical studies on the time scale of fluid flow, heat transfer and hydrate reaction in the fractured GHBS. And the static dimensionless numbers are incapable to capture the spatial and temporal variations of physical fields in GHBS. A comprehensive evaluation framework addressing the interplay among thermal, hydraulic and chemical processes is necessary to further reveal the relationships among these processes and their synergistic effect on gas production at different spatial and temporal scales, especially in the presence of fractures in GHBS.

Therefore, in this study, a dynamic dimensionless analysis framework is employed for methane extraction from fractured GHBS. This framework delineates the complex interplay among hydrate reaction kinetics, fluid flow, and heat transfer across various temporal and spatial scales. To demonstrate the feasibility of the proposed framework, we employ a coupled thermo-hydro-chemical model to conduct numerical simulations under various injection temperature, depressurization, and well spacing conditions. The simulation platform was developed by Ju et al. based on high performance multiphysics code GEOS [34]. This paper is organized as follow. Except for the introduction section, section 2 introduces the mathematical equations and assumptions. Section 3 deducts the dynamic dimensionless numbers and explains their physical meanings. Section 4 describes the numerical cases of methane gas

extraction in fractured GHBS under different injection temperature, production pressure and well spacing. In Section 5, we analyze fluid production, hydrate saturation evolution, and gas extraction efficiency based on numerical simulation results. Section 6 employs the proposed dynamic dimensionless numbers to analyze the multi-field coupled processes and mechanisms. Section 7 summarizes the main findings of the study and discusses their implications for future research.

2. Mathematical equations

The recovery of hydrate is an extremely complicated multi-physics coupled process that involves phase transition, heat transfer, multi-phase flow, geomechanical response, particle transport, etc. [41]. This study primarily concerns the decomposition behavior of hydrates in fractured GHBS under the combined effect of thermal stimulation and depressurization. The following assumptions are adopted to develop the theoretical model. 1. Fluid flow is described by Darcy's law. 2. Heat transfer is governed by thermal conduction and convection. 3. Hydrate is assumed to be pure methane hydrate, and an equilibrium hydrate decomposition model is used. 4. Geomechanical responses are treated as equivalent to pore compression involving the responses in porosity and fluid density due to pressure/temperature variations [42]. 5. Particle transport is ignored. 6. Fractures are represented by porous media with equivalent porosity and permeability. 7. For the purpose of exploring general trends, the spatial random distribution of physical parameters within the model is not currently considered. These assumptions facilitate a comprehensive analysis of the model from three distinct perspectives-fluid flow, heat transfer, and phase transition.

2.1. Mass balance equations

The mass balance equations of gas-water two-phase flow coupled with hydrate decomposition are shown as follows:

$$\frac{\partial(\rho_a\varphi S_a)}{\partial t}-\nabla\cdot\left[\frac{\rho_a k_{ra}k_0}{\mu_a}(\nabla P_a-\rho_a\boldsymbol{g})\right]=\rho_a q_a \tag{1}$$

$$\frac{\partial(\rho_g\varphi S_g)}{\partial t}-\nabla\cdot\left[\left(1+\frac{K_b}{P_g}\right)\frac{\rho_g k_{rg}k_0}{\mu_g}(\nabla P_g-\rho_g\boldsymbol{g})\right]=\rho_g q_g \tag{2}$$

$$P_c=P_g-P_a \tag{3}$$

$$\frac{\partial(\rho_h\varphi S_h)}{\partial t}+\rho_h q_h=0 \tag{4}$$

where the subscripts "a", "g" and "h" represent aqueous phase, gaseous phase and hydrate phase respectively. ρ is the mass density; φ denotes the porosity of GHBS; S is the saturation of the corresponding phase; P is the pressure, while P_c is the capillary pressure; μ is the viscosity; k is the permeability; q is the source and sink; K_b is the Klinkenberg factor. q_a, q_g and q_h are detailed in hydrate kinetic reaction equations from Moridis' work [43].

Following the conventional treatment of reservoir simulators, the medium's porosity is a function of changes in pressure and temperature from reference conditions, as follows

$$\varphi=\varphi_r\exp(\alpha_T\Delta T+\alpha_P\Delta P) \tag{5}$$

where α_T is the thermal expansivity and α_P is the pore compressibility. ΔT and ΔP are the changes of temperature and pressure respectively.

Capillary pressure is calculated using von-Genuchten model [44]. The permeability of GHBS is a function of both porosity and hydrate saturation [45]:

$$k_0=k_{0r}\left[\gamma\left(\frac{\varphi}{\varphi_r}-1\right)\right]\left\{\max\left[\frac{\varphi(1-S_h)-\varphi_c}{\varphi_r-\varphi_c},0\right]\right\}^{\beta} \tag{6}$$

where k_{0r} and φ_r are the intrinsic permeability and porosity respectively; φ_c is the critical porosity where the reservoir becomes impermeable [43]. γ and β are the index parameters.

The relative permeability depends on capillary effect. In the present study, we employ von-Genuchten equation to calculate the relative permeability of aqueous phase (k_{ra}), and Korey's method for the relative permeability of gaseous phase (k_{rg}) [46,47].

2.2. Energy conservation equation

$$\frac{\partial\left[\varphi\left(\rho_a S_a E_a+\rho_g S_g E_g\right)+(1-\varphi)\rho_s C_s T\right]}{\partial t}-\nabla\cdot\left[\frac{\rho_a H_a k_{ra}k_0}{\mu_a}(\nabla P_a-\rho_a\boldsymbol{g})\right]$$
$$-\nabla\cdot\left[\left(1+\frac{k_b}{P_g}\right)\frac{\rho_g H_g k_{rg}k_0}{\mu_g}\left(\nabla P_g-\rho_g\boldsymbol{g}\right)\right]+\nabla\cdot(\lambda\nabla T)+q_T=0 \tag{7}$$

where E_a, E_g are the specific internal energy of aqueous and gaseous phases, and H_a and H_g are the enthalpy of the two phases respectively; q_T is the energy source and sink owing to hydrate reaction; λ is the composite thermal conductivity of the reservoir, which can be calculated as the volume averaged thermal conductivity of each phase constituent.

2.3. Equivalent permeability and porosity of fracture elements

Fracture is represented as a thin layer of porous media in the developed model, with equivalent permeability k_f and porosity φ_f calculated as follows [48]

$$k_f=\frac{A^3}{12D} \tag{8}$$

$$\varphi_f=\frac{A}{D} \tag{9}$$

where A is the fracture aperture and D is the thickness of fracture elements.

3. Dimensional analysis

Teng et al. derived classical dimensionless numbers considering the competition between mass-heat transfer processes and hydrate reaction, which can be represented mathematically as the Damköhler numbers, and listed as Da^a, Da^a, Da^{Ta}, Da^T [38]. The derivation process and specific expressions for these five Damköhler numbers are provided in Appendix A.

These dimensionless numbers serve as a source of motivation for subsequent investigations, albeit with notable limitations. Specifically, the Damköhler numbers alone fail to quantify the relative magnitudes of fluid convection and thermal conduction. Furthermore, these parameters remain constant throughout the evolution process and therefore incapable of capturing the relative relationship of physical fields across different temporal and spatial domains during gas production. Finally, the spatial and temporal evolution of flow field may be altered by the presence of fractures, an effect that is not accounted for the Damköhler numbers. To circumvent these limitations, the present study proposes a set of dynamic characteristic times obtained from the governing equations, from which five dynamic dimensionless parameters are subsequently derived. These dynamic characteristic times are intrinsically the dimensionless time required for the depletion of a certain physical quantities (e.g., mass, energy) at the corresponding consumption rate (e.g., hydrate decomposition rate, convective rate, thermal conductivity rate):

$$\tau_{c,a}=\frac{\rho_a\varphi S_a L}{\rho_a v_a t}=\frac{\varphi S_a L\mu_a d_f}{k_{ra}k_0(P-P_b)t_r} \tag{10}$$

$$\tau_{c,g}=\frac{\rho_g\varphi S_g L}{\rho_g v_g t}=\frac{\varphi S_g L}{\frac{k_{rg}k_0(P+P_c-P_b)}{\mu_g d_f}t_r} \tag{11}$$

$$\tau_{tc,a}=\frac{\left[\varphi\left(\rho_a S_a E_a+\rho_g S_g E_g\right)+(1-\varphi)\rho_s C_s T\right]L}{\rho_a v_a H_a t_r} \tag{12}$$

$$\tau_{tc,g}=\frac{\left[\varphi\left(\rho_a S_a E_a+\rho_g S_g E_g\right)+(1-\varphi)\rho_s C_s T\right]L}{\rho_g v_g H_g t_r} \tag{13}$$

$$\tau_{hc}=\frac{\left[\varphi\left(\rho_a S_a E_a+\rho_g S_g E_g\right)+(1-\varphi)\rho_s C_s T\right]Ld_f}{\lambda(T_b-T)t_r} \tag{14}$$

$$\tau_{t,h}=\frac{\left[\varphi\left(\rho_a S_a E_a+\rho_g S_g E_g\right)+(1-\varphi)\rho_s C_s T\right]}{q_h\Delta H t_r} \tag{15}$$

$$\tau_h=\frac{\rho_h\varphi S_h}{M_h q_h t_r} \tag{16}$$

where t_r is the reference time. Each of the characteristic times, namely τ_c, τ_{tc}, τ_{hc}, $\tau_{t,h}$, and τ_h, possesses a distinct physical significance. Specifically, τ_c signifies the dimensionless time required for the complete depletion of fluid under the current flow rate. τ_{tc} refers to the dimensionless time needed for complete heat loss of the system under the current thermal convection rate. τ_{hc} represents the dimensionless time required for the complete heat loss of the system through conduction, considering the current heat conduction efficiency. $\tau_{t,h}$ is the characteristic time required to consume the heat in the reservoir according to the current rate of hydrate decomposition. τ_h signifies the dimensionless time necessary for the complete consumption of hydrate by the system at the current hydrate reaction rate. The dynamic dimensionless numbers can be established based on these characteristic times. Notably, particular attention should be given to the fracture, such that the flow velocity and Fourie heat transfer is correlated to the longitudinal distance from the fracture, denoted as d_f. In the processes involving mass and heat transfer, aqueous plays a more significant role than gaseous. Therefore, this article focuses primarily on analyzing the characteristic time of aqueous.

$$R_1=\frac{\tau_{c,a}}{\tau_h}=\frac{\mu_a S_a M_h q_h L d_f}{k_{ra}k_0(P-P_b)\rho_h S_h} \tag{17}$$

$$R_2=\frac{\tau_{hc}}{\tau_{tc,a}}=\frac{\rho_a k_{ra}k_0(P-P_b)H_a}{\mu_a\lambda(T_b-T)} \tag{18}$$

$$R_3=\frac{\tau_{tc,a}}{\tau_{t,h}}=\frac{\mu_a q_h\Delta H L d_f}{\rho_a k_{ra}k_0(P-P_b)H_a} \tag{19}$$

$$R_4=\frac{\tau_{hc}}{\tau_{t,h}}=\frac{\Delta H q_h L d_f}{\lambda(T_b-T)} \tag{20}$$

Besides, Prandtl number is wildly used to describe the ratio of momentum diffusivity and thermal diffusivity, so we employ this number as a comparison:

$$P_r=\frac{\left(\mu_a C_{p,a}+\mu_g C_{p,g}\right)}{\lambda} \tag{21}$$

With the exception of R_2 and P_r, these dimensionless variables have corresponding relationships with the Damköhler numbers derived earlier.

4. Numerical simulation

4.1. Model setup

The Shenhu Area is situated near the southeast of the Shenhu Underwater Sandy Bench, located along the central region of the north slope of the South China Sea. In May of 2007, significant scientific progress was made during a research expedition led by the China Geological Survey at sites SH2, SH3, and SH7 within the Shenhu Area of the northern South China Sea, wherein GHBS samples were successfully collected [49]. This noteworthy discovery marked the initial instance of an abundant hydrate found in the northern region of the South China Sea, thereby designating Shenhu as a vital strategic site for potential gas hydrate exploitation throughout China. The subsequent production test in 2017 and 2020 also confirmed the gas production potential from hydrate [3,50].

This study employed the GEOS_Hydrate simulator [34], which is developed based on GEOS [51] and has been validated in the second International Gas Hydrate Code Comparison Study [52].

Based on the geological model of the marine hydrate reservoir, a conceptual model and the corresponding planar computational model are derived in this study (Fig. 1). The GHBS are surrounded by extremely low permeable overburden and underburden layers. To enhance recovery efficiency, this study employs a horizontal well system, and the heat injection sites and depressurization sites are located at different horizontal wells.

To capture the multi-physics process and clarify the mechanisms behind them, it is acceptable to use a simple planar model that only contains the key features, namely the injection well, production well, and the fractures. The planar model was established, with the initial well spacing of 200 m (set as *x*-direction), and the fracture spacing of 150 m (set as *y*-direction), and the thickness of 30 m (set as *z*-direction). The local grid refinement was applied surrounding the wells and fractures with the grid's resolution of 0.1 m. The number of grid blocks in the *x*-direction was set to 132 align with the initial well spacing while the *y*-direction contained 105 grid blocks, resulting in a cumulative usage of 13,860 grid blocks.

4.2. Initial and boundary conditions

The numerical model resembles the condition in Shenhu area, South China Sea [34,53]. Table 2 listed the key parameters of this area.

To evaluate the short-term and long-term reservoir evolutionary patterns under different recovery strategies, this study analyzed the GHBS temperature, pressure, and phase saturation over a decade under varying pressure drop (3 MPa–8 MPa), heat injection temperature (10 °*C* - 90 °*C*), and well spacing (50 m–300 m). We choose hot water as the heat injection fluid with a fixed injection rate of 0.025 kg/s. To avoid numerical inconsistency and divergency, instead of applying the target injection temperature immediately at the injection well, we gradually increase the injection temperature from the initial value (10 °*C*) to the target value linearly within 10^6 s. The imposition of no-flux boundary conditions on the elemental components situated along the four external edges of the computational domain is settled. Moreover, the thermal interactions with the overburden and under-burden remain unaccounted for, which may result in the failing of matching historical production data. These simplifications are made to tentatively offer a starting point for research.

5. Simulation results

In this chapter, we present simulation results under various production pressure, injection temperature, and well spacing in terms of gas production, water production, heat production, temperature variation, and pressure evolution. We then evaluate the gas production under different conditions.

5.1. influence of production pressure (P_{prod})

Low production pressure not only disrupts the equilibrium condition of gas hydrates and leads to hydrate decomposition, but also induces a pressure gradient between injection and production wells to drive fluid

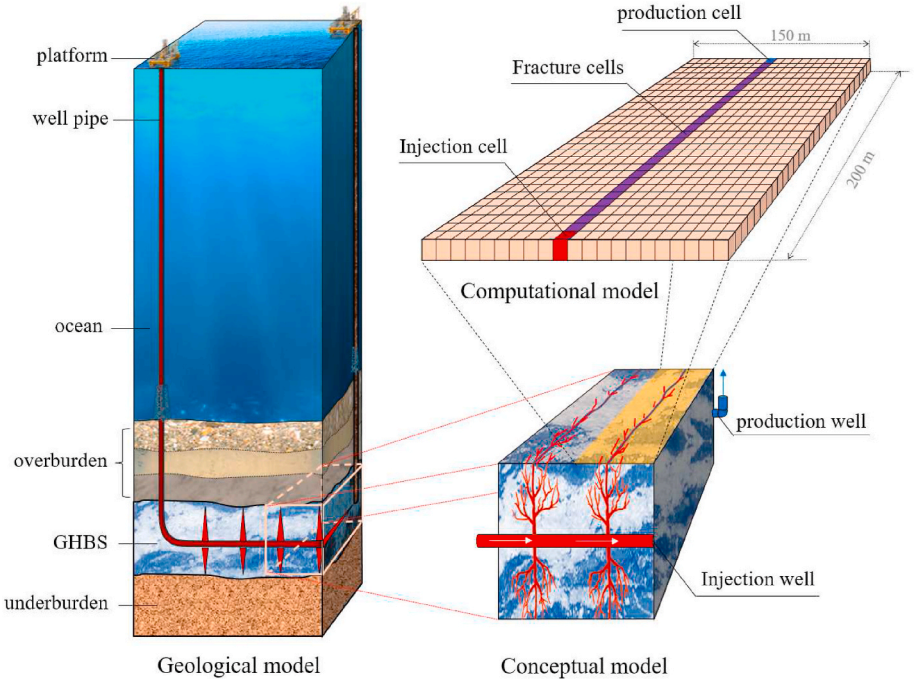

Fig. 1. Schematic diagram of combining depressurization-heat injection-fracturing methods to recover gas from GHBS in dual-horizontal well system: from geological model to computational model. Left: geological model. Right-bottom: conceptual model where both the overburden and underlying burden are impermeable. Right-uppermost: computational model reduced to a 2D plane.

extraction. This section summarizes the production performance of gas hydrate reservoirs under production pressures of 3 MPa, 4 MPa, 5 MPa, 6 MPa, 7 MPa and 8 MPa. The injection temperature is fixed at 50 °*C*. The production pattern of methane gas varies greatly under different production pressures (Fig. 2a). When the production pressure is under 6 MPa, the methane production rate is relatively high at the commencement of simulation and then gradually decreases. When the production pressure is over 6 MPa, the methane production rate is relatively low at the beginning, and then gradually increases, reaching a peak after approximately 10 days, and then decreases. One possible explanation for this phenomenon is that, in the early stages of production, the heat supplementation near the production well is insufficient, and the endothermic decomposition of gas hydrates due to depressurization causes a local temperature drop near the decomposition front. The temperature in this region may fall below the stability threshold of gas hydrates, resulting in the cessation of decomposition of gas hydrates under the current production pressure, unless additional thermal energy is supplied. This phenomenon is called self-preservation effect, which is more likely to occur when the production pressure exceeds 6 MPa [6]. After about 1000 days, the production rates of methane gas at different production pressures are almost identical, meaning that the production pressure is no longer the dominant factor affecting gas production. The cumulative gas production also varies greatly with different production pressures, i.e., 3.23×10^5 STP m^3, 2.268×10^5 STP m^3, 1.52×10^5 STP m^3, 1.046×10^5 STP m^3, 9.037×10^4 STP m^3, and 8.016×10^4 STP m^3 at 3 MPa, 4 MPa, 5 MPa, 6 MPa, 7 MPa, and 8 MPa respectively (Fig. 2a). The gas production potential at 3 MPa is twice that at 5 MPa, and four times that at 8 MPa. Reducing production pressure can greatly increase production, but when the production pressure decreases to 2 MPa or below, ice will appear in the reservoir and impede gas production [54], and the multi-field process become more complex [55]. But ice formation is not the primary focus of this article, and to avoid additional

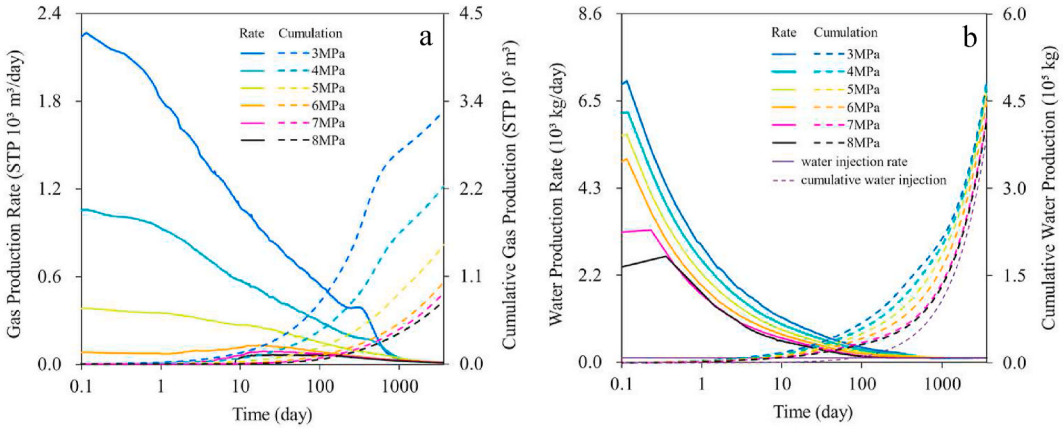

Fig. 2. The production rate and the cumulative production of fluid at different production pressure. a: methane gas mass production. b: water mass production and injection. Solid lines: mass rate. Dashed lines: cumulative mass production or injection. Purple solid line in b: water mass injection rate. Purple dashed line in b: cumulative water mass injection. (For interpretation of the references to colour in this figure legend, the reader is referred to the Web version of this article.)

complexities associated with ice formation, we will temporarily exclude scenarios where the operating pressure is below 3 MPa. The cases with a lower production pressure exhibit higher water production rates before approximately 300 days. However, beyond that time, all cases experience a decline in water production rate, ultimately approaching the water injection rate (Fig. 2b). Fig. 2 reveals that production pressure mainly impacts the short-term gas and water production behavior (within 1 year). In subsequent sections, we will further analyze that dominance effect of injection temperature on long-term production behavior.

Heat production rates with different pressure show considerable consistency. As the injection temperature gradually increases to 50 °C in 10^6 s, the deviation temperature dT gradually increases to a peak and then decreases. In the late period, the injection temperature remains constant at 50 °C, and therefore the decreases of dT is mainly caused by the increase in production temperature. Since hydrates decomposition is an endothermic process, the increase of production temperature indicates that the injected heat is not completely utilized by GHBS, and is transferred to the production well through fracture by hot fluid flow. Such a phenomenon is named thermal breakthrough, an important indicator of energy waste [34]. It is important to properly delay thermal breakthrough to improve energy utilization efficiency. As shown in Fig. 3b, the blue and red arrows annotate the onset points of thermal breakthrough at 3 MPa and 8 MPa, respectively. Increasing the production pressure will simultaneously postpone thermal breakthrough and impair the gas production, so further analysis is conducted to clarify the influence of production pressure on hydrate decomposition. The variation of gas hydrate saturation is an intuitive indicator for evaluating the effectiveness of reservoir exploitation, and gas hydrate saturation will directly affect the permeability, heat conductivity, and geomechanical properties of GHBS. In Fig. 4, during gas production, hydrate decomposition first occurs near the fracture due to the relatively low pressure and high temperature in the fracture, leading to the formation of a hydrate-free zone (HFZ) where hydrate is disappeared. The HFZ gradually expands towards model boundaries, dividing the reservoir into two regions: the HFZ and the background zone (BGZ). Within HFZ, hydrate completely decomposes and results in a highly permeable fluid flow in this region. In contrast, the hydrate saturation in BGZ remains relatively high, and the permeability is therefore lower than that in HFZ. Overall, the production pressure shows little effect on the evolution of HFZ, but it will significantly impact the evolution of BGZ. At low production pressures (<5 MPa), the overall hydrate saturation in BGZ gradually decrease over time. While at high production pressures (>5 MPa), the hydrate saturation of BGZ remains almost constant, and even slightly increases at 7 MPa and 8 MPa scenarios. The increase of hydrate saturation indicates the occurrence of secondary hydrate formation within BGZ. Such a hydrate formation process actually means a negative contribution of gas production from BGZ, manifesting as the negative value in Fig. 5. Saturation variation in BGZ produces the main variation of gas production at different production pressures; while the variation of gas production in HFZ at different production pressures is relatively minor (Fig. 5). A positive gas production contribution in BGZ indicates that the hydrate in BGZ is decomposing and producing gas on a general basis (production pressure at 3 MPa, 4 MPa and 5 MPa). Conversely, a negative gas production contribution in BGZ suggests that secondary hydrate is being generated in BGZ, thereby consuming the produced gas from HFZ (production pressure at 7 MPa and 8 MPa).

The simulation zone can be divided into two background zone (BGZ) and hydrate-free zone (HFZ) according to the hydrate saturation. Changing the production pressure mainly influences the hydrate saturation of BGZ.

The solid lines are the gas production contribution of HFZ, and the dashed lines are that of BGZ. The purple dashed line represents the critical curve where the gas contribution from the BGZ reaches zero. Below this curve, it indicates that the corresponding BGZ exhibits negative gas contribution, signifying the presence of secondary gas hydrate production.

5.2. The influence of injection temperature (T_{inj})

Injecting hot water supplies heat for hydrate decomposition, a endothermal process, and the supplication efficiency is controlled by the injection temperature when the water flux is fixed. In this subsection, we analyze the production performance under injection temperatures of 10 °C, 20 °C, 40 °C, 50 °C, 60 °C, 80 °C, and 90 °C with a fixed production pressure of 5 MPa. Two different temporal stages are identified from the gas production rate curves (Fig. 6). In the initial stage, gas production rate is almost identical for different injection temperatures. In the middle and later stage, the gas production rate increases with injection temperature, resulting in a significant difference in cumulative gas production (Fig. 6). The total gas production for $T_{inj} = 90$ °C is about 2.5 times that for $T_{inj} = 10$ °C. Specifically, the ten-year cumulative gas production is 7.293×10^4 STP m^3, 1.097×10^5 STP m^3, 1.421×10^5 STP m^3, 1.52×10^5 STP m^3, 1.602×10^5 STP m^3, 1.727×10^5 STP m^3, and 1.787×10^5 STP m^3 when the injection temperatures are 10 °C, 20 °C, 40 °C, 50 °C, 60 °C, 80 °C, and 90 °C respectively. The water production rate and the cumulative water production are almost the same at different injection temperatures (Fig. 6b). In practical applications, it is

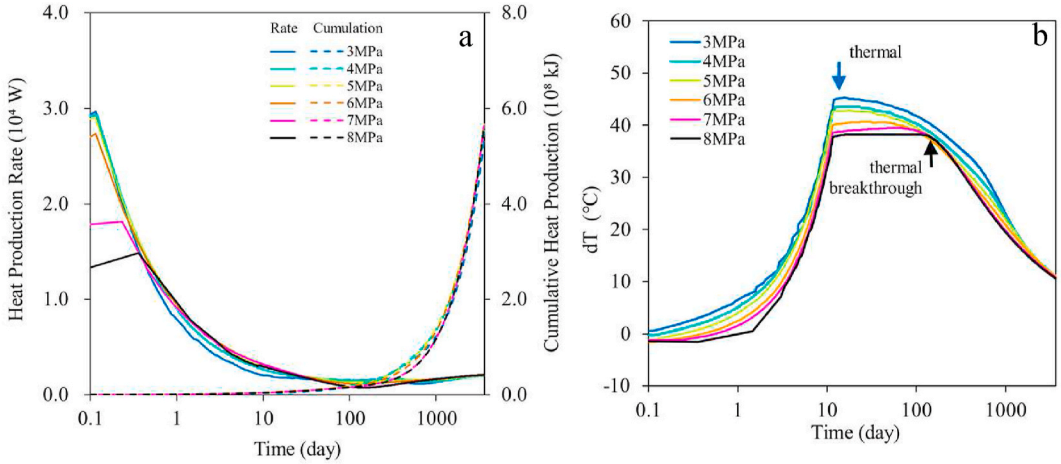

Fig. 3. The heat production and the deviation of injection temperature with production temperature at different production pressure. a: heat production rate and cumulative heat production; b: deviation temperature, that is injection temperature subtracts production temperature (d$T = T_{inj} - T_{prod}$). The drop-down point of dT indicates arrival of the thermal breakthrough.

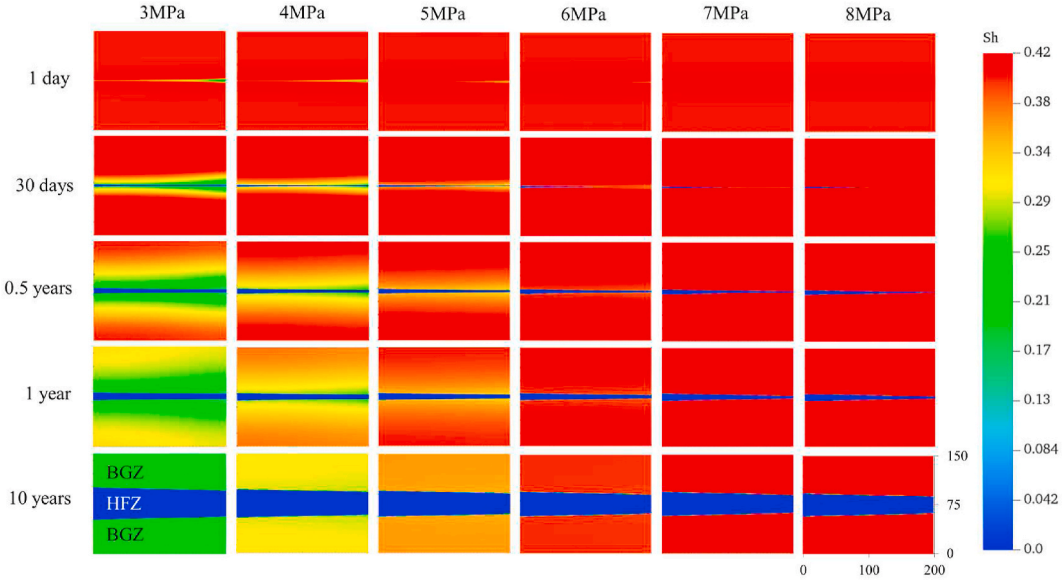

Fig. 4. Hydrate saturation distribution across multiple production stages under different production pressure.

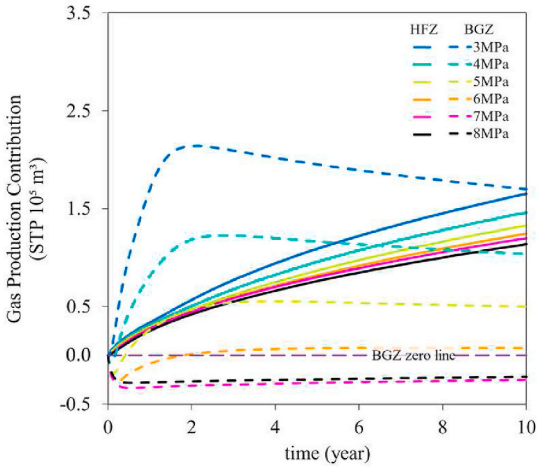

Fig. 5. The gas production contribution of HFZ and BGZ at different production pressures.

necessary to minimize water production to control production costs, so increasing the injection temperature is efficient to enhance gas production and suppress water production. However, it is important to note that raising the injection temperature results in bringing thermal breakthrough forward and amplifying energy dissipation, which is demonstrated by an increase in heat production (Fig. 7a).

Hydrate formation or decomposition occurs synchronously at different locations in BGZ, because the hydrate saturation within BGZ shows a nearly uniform variation. The response of HFZ to different exploitation conditions is to alter HFZ area. Therefore, the implementation of appropriate techniques to enhance production becomes crucial in reducing hydrate saturation within the BGZ and expanding the area of the HFZ, which ultimately facilitates the decomposition of hydrates. The injection temperature shows no effect on the temporal evolution of hydrates within BGZ, as the saturation levels within BGZ at different injection temperatures are nearly identical during the same time period, while increasing injection temperature expands the area of HFZ (Fig. 8). The gas production contribution from BGZ and HFZ is correspondent to this phenomenon above (Fig. 9). The contribution of gas production from BGZ varies slightly with different injection temperatures, but the contribution from HFZ changes significantly when injection temperature changes. The results complement the effects caused by changing production pressure that depressurization mainly

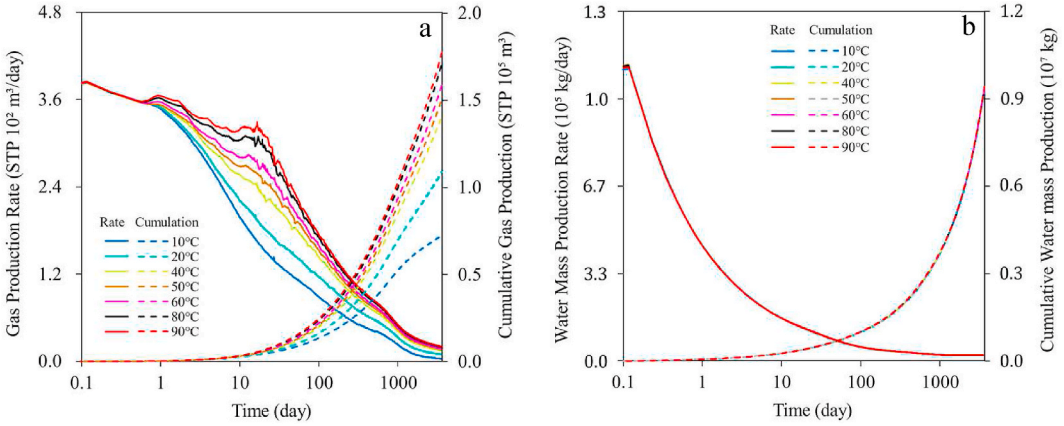

Fig. 6. The production rate and the cumulative production of fluid at different injection temperature. a: gas mass production; b: water mass production. Solid lines: production rate. Dashed lines: cumulative production.

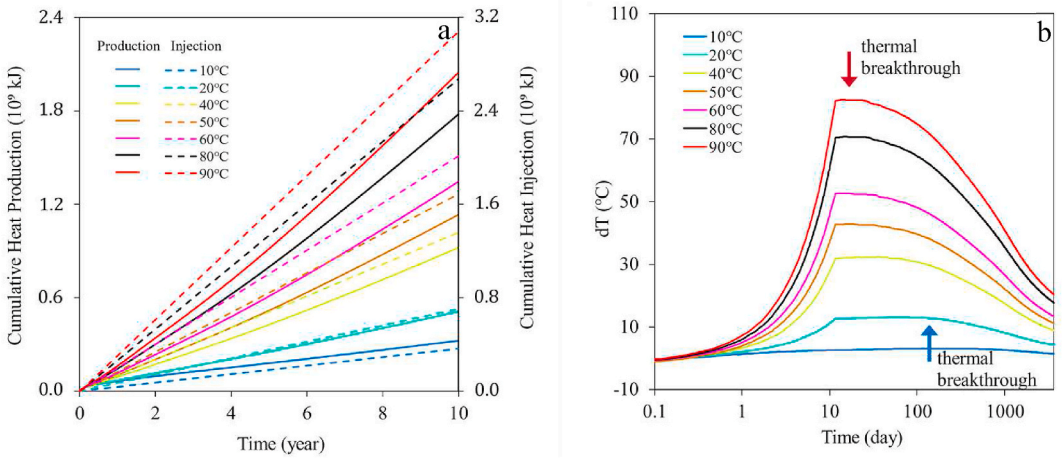

Fig. 7. The heat injection and production along with the deviation between injection and production temperatures under various injection temperature. a: cumulative heat production and cumulative heat injection; b: deviation temperature (as defined in Fig. 3).

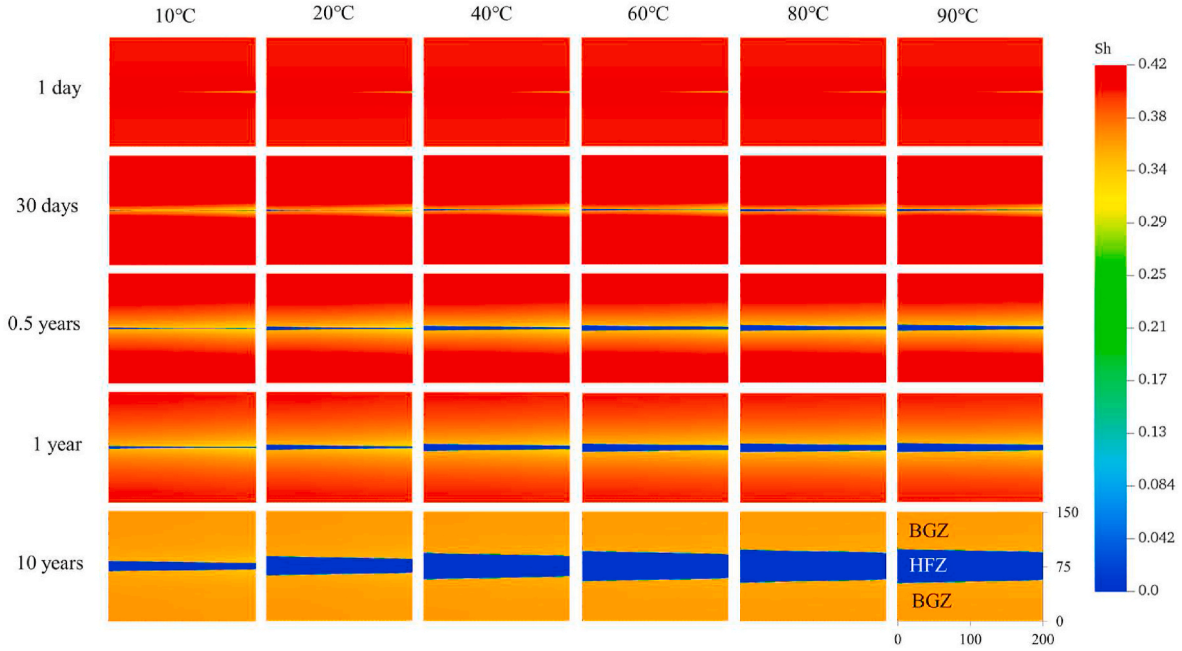

Fig. 8. The hydrate saturation distribution across various production stages under different injection temperatures.

affects BGZ, and show minor effects on HFZ, which has been discussed in 5.1. In the first half-year of exploitation, the gas contribution from BGZ is negative, indicating the formation of secondary hydrate within this zone. This phenomenon may be attributed to inadequate heat supply, forming a low-temperatures zone in the vicinity of HFZ.

5.3. *The influence of the well spacing (L_{ws})*

The above analyses indicate that the production pressure mainly affects BGZ, while the injection temperature primarily affects the HFZ. Such a phenomenon is governed essentially by the coupled interaction between fluid flow and heat transfer processes. This subsection aims to investigate the coupling relationship between flow and thermal conduction under different well spacings (i.e., model size) from 50 m to 300 m. The injection temperature and production pressure are fixed at 50 $^{\circ}C$ and 5 MPa respectively. The cumulative gas production increases proportionately with well spacing. Conversely, the water production rate is basically controlled by the injection rate and reservoir size, so the water production across different well spacings shows minor differences than gas production. After approximately 1000 days, the water production rates converge towards the injection rate (the solid purple line in Fig. 10b).

At the initial stage of gas production, a larger well spacing exhibits higher heat production rate due to the larger scale of the model, accompanying with a higher water production and heat discharge. However, in the later period, the relationship between well spacing and heat production reverses and a smaller well spacing exhibits higher heat production rate. Such a notable transition occurs at approximately 110 days, and mainly coursed by the increase of production temperature, that is thermal breakthrough. For the narrower well spacing case, thermal breakthrough arrives earlier (Fig. 11b). GHBS with a narrow well spacing shows a low gas yield and a high energy waste, so it is benefit to exploit the reservoir with a larger well spacing, and the injection and production wells should be connected with fractures. However, the well spacing is limited by the hydraulic fracturing techniques in realistic applications. Well spacing has a relatively minor impact on

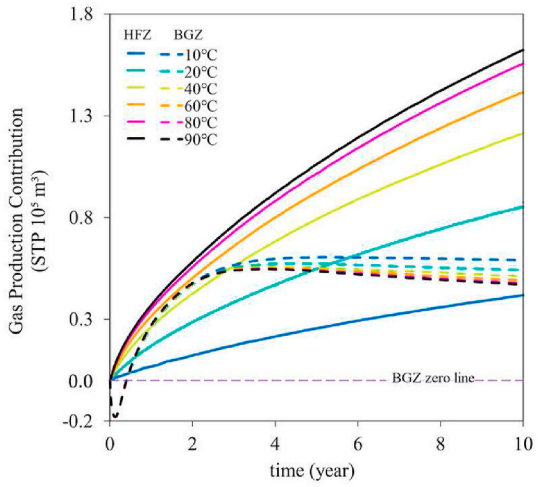

Fig. 9. The gas production contribution curves of HFZ and BGZ under different injection temperatures (BGZ zero line is defined in Fig. 5).

both HFZ and BGZ (Fig. 12 & Fig. 13).

6. Analysis and discussion

6.1. Insights from dynamic dimensionless numbers

The numerical simulations reveal the roles of depressurization and heat injection in extracting gas from fractured GHBS. In this subsection, we employ the dynamic dimensionless numbers proposed in Section 4 to further analyze how multiple-field coupled processes affect the gas production. We show the distribution of 5 dimensionless numbers corresponding to production pressures of 3 MPa, 5 MPa, 8 MPa, and injection temperatures of 10 °C, 50 °C and 90 °C (Fig. 14). The distribution of these 5 dynamic dimensionless numbers is closely depend on hydrate saturation, and can also be roughly divided into two zones which resemble the BGZ and HFZ defined for hydrate saturation. In BGZ, the reaction rate of hydrate decomposition is much faster in terms of mass transport and heat transfer, as evidenced by the corresponding dynamic dimensionless numbers R_1, R_3, and R_4 (much greater than 1). However, within HFZ, R_1, R_3, and R_4 are all close to zero as there is no hydrate decomposition at all. P_r is widely used to capture the relative importance of momentum diffusivity (viscosity) and thermal diffusivity. The concepts of R_2 bear considerable resemblance with P_r, but R_2 represents the actual magnitude of thermal conduction and convection. In other words, R_2 builds upon P_r by considering the effects of pressure and temperature gradients. P_r represents the potential for occurring convective heat

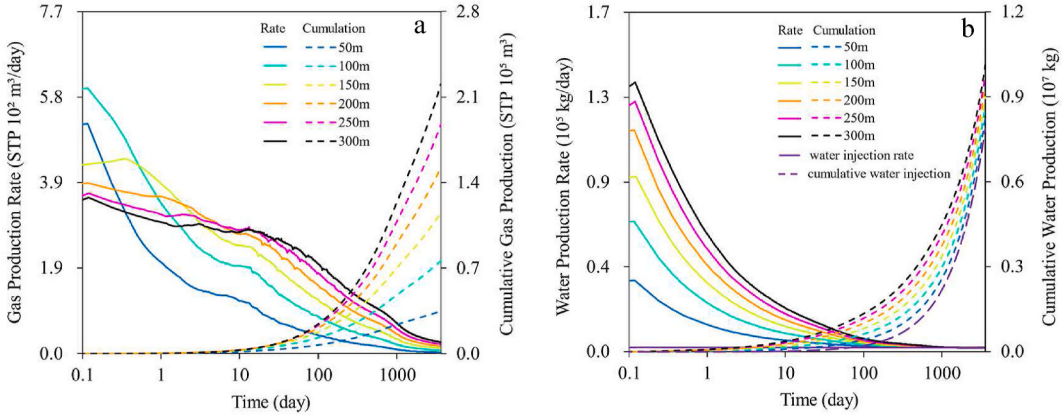

Fig. 10. The production rate and the cumulative production of fluid with different well spacing. b: water mass production. Solid lines: production rate. Dashed lines: cumulative production.

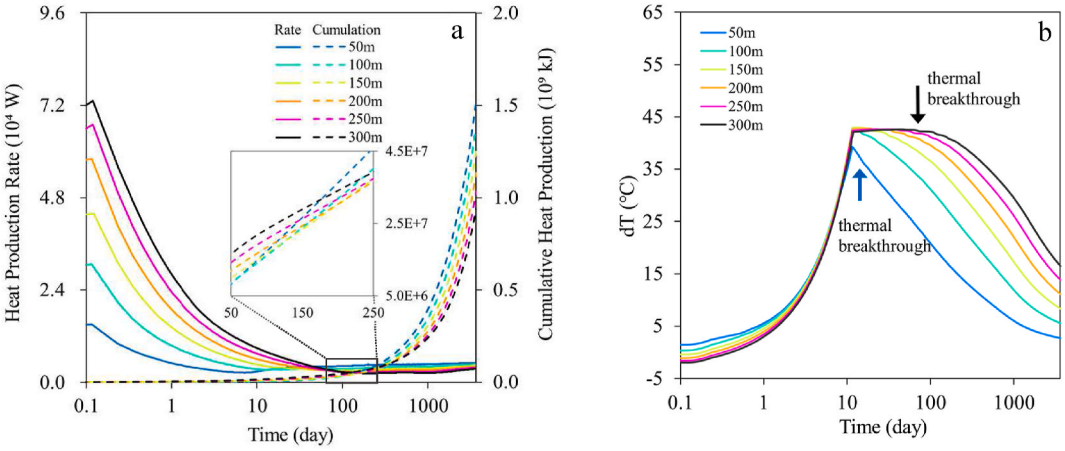

Fig. 11. The heat production and the deviation of injection temperature with production temperature with different well spacing. a: differential and cumulative heat production; b: deviation temperature (as defined in Fig. 3).

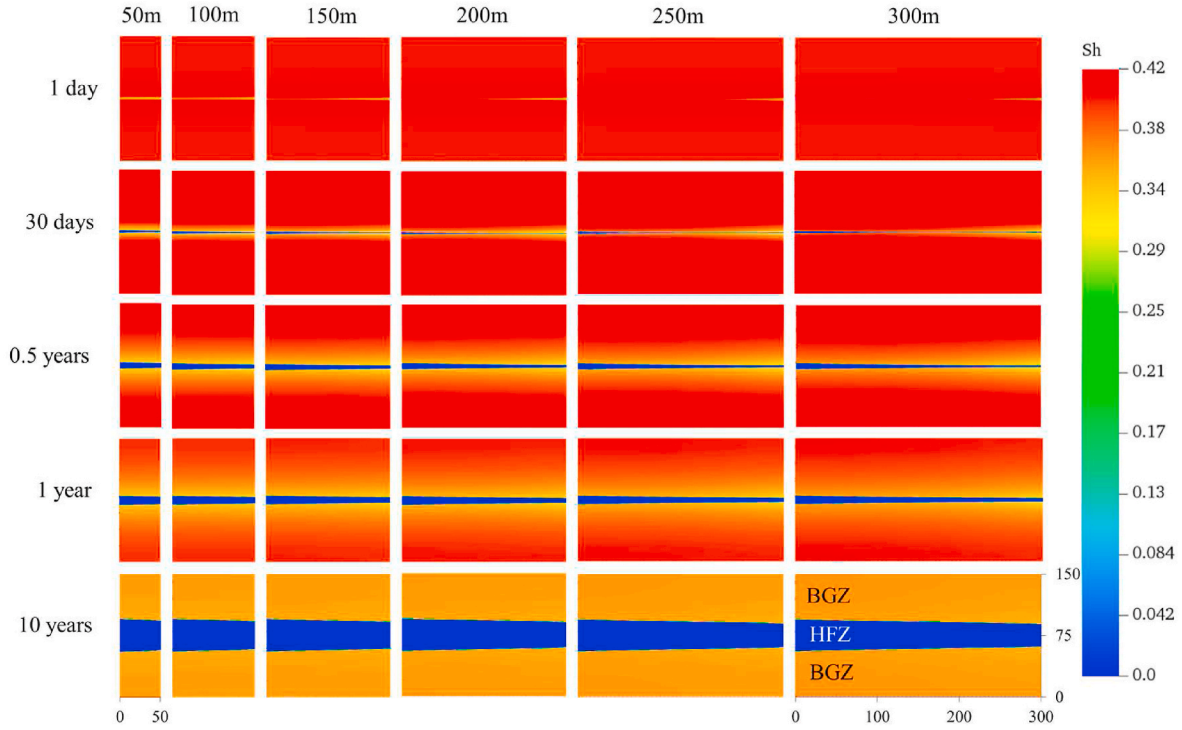

Fig. 12. The hydrate saturation distribution during varies production stages with different well spacings.

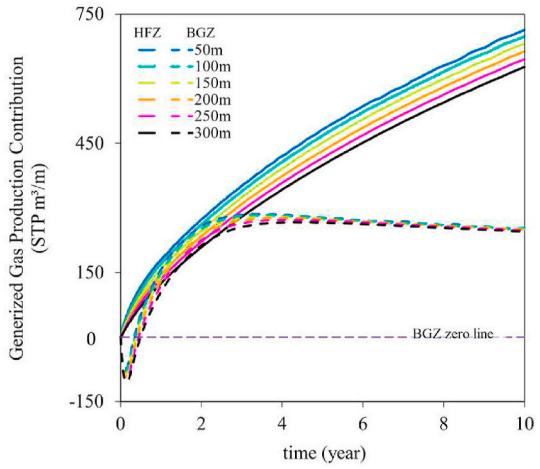

Fig. 13. The gas production contribution curves of HFZ and BGZ with different well spacings (BGZ zero line is defined in Fig. 5).

transfer and thermal conduction, but it may not accurately depict the actual occurrence of these two processes (see Fig. 15).

The red region in P_r plot indicates that conductive effect dominates heat transfer in the red region, and convection effect dominates heat transfer in the blue region. Therefore, to accelerate hydrate decomposition in the red region, increasing the heating temperature is effective as a higher temperature gradient induces more significant thermal conduction. For the blue region, reducing production pressure (i.e., increasing pressure gradient) can enhance heat convection and therefore enhance gas production.

The distribution of R_2 reveals that thermal conduction is the main limit factor within HFZ, whereas heat convection is the main limit factor within BGZ. According to Fig. 14, the conclusions derived from P_r and R_2 are inconsistent and even contradictory to each other. The discrepancy is arisen mainly by two sources. Firstly, the decomposition of hydrates leads to a substantial increase in local permeability. Secondly, significant non-uniformity in pressure gradients exists across different temporal and spatial positions. R_2 encompasses both sources of discrepancy, whereas P_r does not take them into account. So, in this problem, R_2 is more persuasive and accurate to capture the relation of convective heat transfer and thermal conduction. According to R_2, thermal conduction is the limiting factor in HFZ, while fluid convection is the limiting factor in BGZ. R_2 explains why changing injection temperature has obvious impacts on HFZ, while alternating production pressure significantly affects BGZ.

As a comparison, we demonstrate the key dynamic parameters at the early gas production stage (10 days). In the early stages of GHBS exploitation, the primary limiting factor is thermal conduction instead of fluid flow, and the controlling relation is more obvious when the pressure drop is not particularly small (except for 8 MPa) or the injection temperature is not significantly high (except for 90 °C). The early stage shows different coupling relation with the later stages, because the pressure gradient in the early stage is relatively high, resulting in a high flow velocity. Therefore, in the early stages of GHBS exploitation, fluid flow predominates both in BGZ and HFZ. In the later stages of exploitation, flow velocity is the primary limiting factor within BGZ, while heat transfer dominates within HFZ, which controls the expansion of the hydrate decomposition front.

We further analyze the distribution of R_2 with different well spacings and in different gas production stages (Fig. 16). The variations in well spacing do not affect the distribution feature of R_2. It provides a further explanation for the conclusion reached in subsection 5.3 that enlarging the well spacing will not affect the gas recovery efficiency, but will increase the total gas production.

Notably, R_1, R_3, and R_4 are directly proportional to the square of the model scale, as shown in Eq. 22, 24, 25. This suggests that at small scales (e.g., reactor vessel scale), the rate of hydrate reaction may be comparable to the rates of heat transfer and fluid flow, where the rate of hydrate reaction could become the limiting factor. However, both P_r and R_2 are scale-independent and mainly depends on the intrinsic properties of the reservoir, and therefore these two dimensionless numbers are applicable to the analysis of models with any spatial scale.

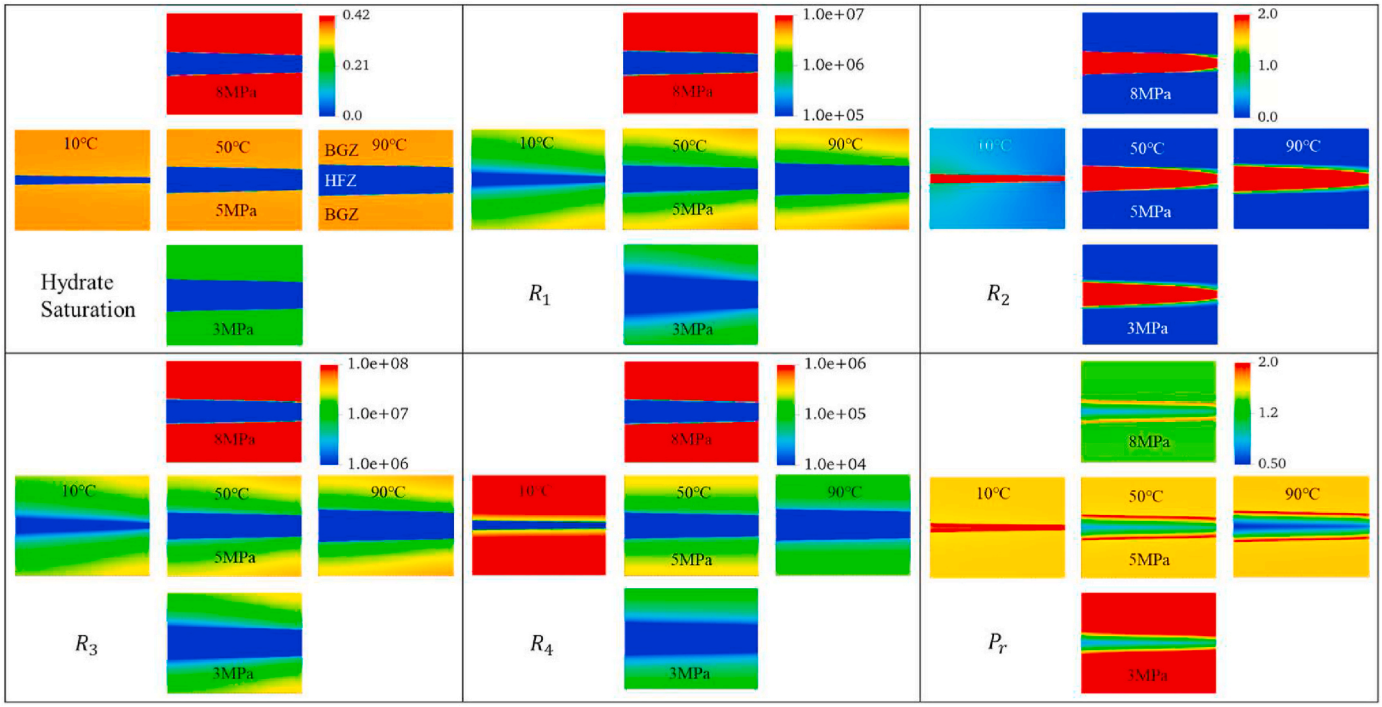

Fig. 14. The distribution of proposed dynamic dimensionless numbers under the conditions of injection temperature of 10 °*C*, 50 °*C* and 90 °*C*, and production pressure of 3 MPa, 5 MPa, 8 MPa, after 10 years of gas production.

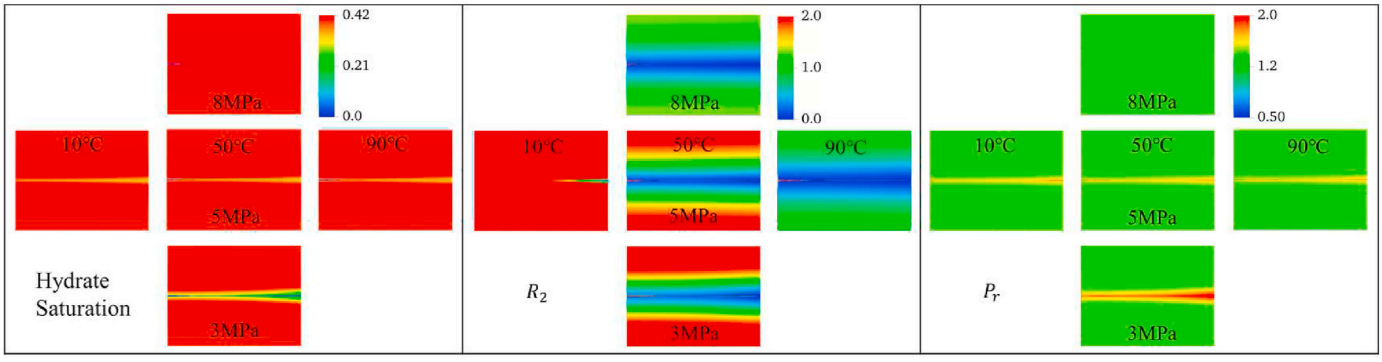

Fig. 15. The distribution of R_2 and P_r under the conditions of injection temperature of 10 °*C*, 50 °*C* and 90 °*C*, and production pressure of 3 MPa, 5 MPa, 8 MPa, after 10 days of production.

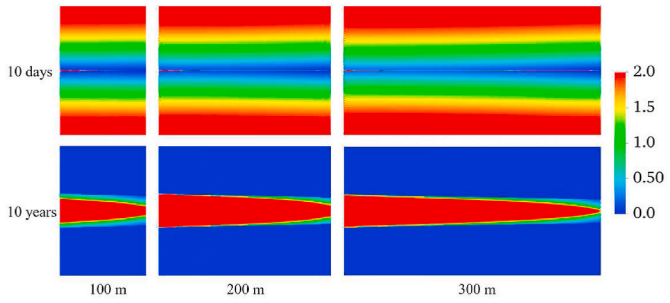

Fig. 16. The distribution of R_2 with different well spacing at 10 days and 10years.

6.2. *Estimating production stages using* R_2

In the above section, R_2 is proven an effective factor for quantifying the relationship between heat transfer and fluid flow. R_2 also provides insights into the optimization strategy of gas production from fracture GHBSs. For instance, when R_2 is significantly less than 1, heat transfer becomes the primary controlling factor and fluid flow is the limiting factor. In such a scenario, decreasing production pressure helps to further increase gas production. Conversely, when R_2 is significantly greater than 1, fluid flow becomes the primary controlling factor, and increasing injection temperature is effective to enhance gas production. However, R_2 varies over time and space. We further analyze the variations of R_2 in BGZ and HFZ separately over time (Fig. 17). R_2 in BGZ is greater than 1 initially and gradually decreases below 1 for all cases (Fig. 17a), Fluid flow plays a primary controlling role in the early stages of exploitation, whereas in later stages, heat transfer becomes the primary control factor. The transition time between the two modes highly depends on operation parameters, especially the injection temperature. At lower injection temperatures, the transition from a flow-controlled mode to heat transfer-controlled mode happens at late stage of the production (about 350 days for 10 °*C*). Conversely, at high temperatures, this transition can be completed within a few days (about 2 days for 90 °*C*). Production pressure also affects the transition time. Larger

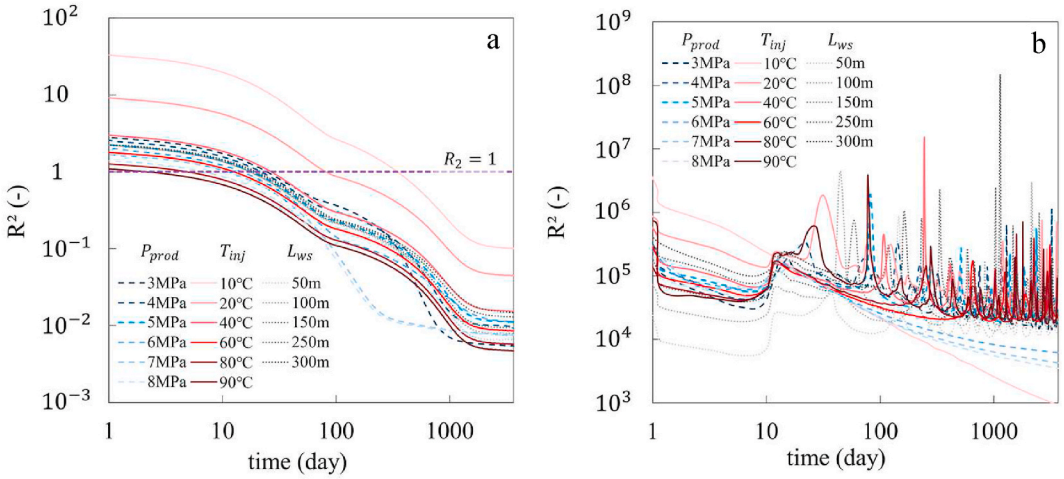

Fig. 17. The temporal evolution of the mean R_2 values in BGZ and HFZ is the subject under consideration. a: R_2 in BGZ; b: R_2 in HFZ.

production pressure induces earlier transition from flow-controlled mode to heat transfer-controlled mode. The impact of well spacing on transition time is relatively minor. Referring to the definition of R_2 in Table 1, it can be concluded from Fig. 17b that in HFZ fluid flow is the limiting factor in the region under different production conditions. The disappearance of hydrate in HFZ will exceptionally enhance the absolute permeability of the medium, thus promoting fluid flow in HFZ.

6.3. Improving gas recovery efficiency using R_2

Previously, we utilize the concept of dynamic dimensionless numbers to elucidate the relationships between fluid flow and thermal conduction. However, in the context of practical engineering applications, there is a demand of clarifying the relationship between production conditions and gas recovery efficiency. This section summarizes the gas recovery efficiency obtained from different numerical simulation cases. Both decreasing production pressure and increasing injection fluid temperature can increase the gas recovery rate, but the mechanisms are distinct. As discussed in sections 5.1 and 5.2, reducing production pressure will increase the hydrate decomposition from BGZ, while increasing injection temperature will increase the hydrate decomposition from HFZ. Unlocking the limiting factor helps to increase the gas recovery efficiency of GHBS, and the parameter R_2 serves as a precise indicator of these limiting factors. The value of R_2 is independent of model size, and thus altering well spacing cannot direct impact gas recovery efficiency, which is consistent with the simulation result in Fig. 18c. With the reference of R_2 evolution in section 6.2, to further increase the gas recovery efficiency, we can take strategies to enhance the fluid flow in BGZ or increase the thermal conduction in HFZ. In addition to increasing injection temperature and reducing production pressure, reservoir modification can be employed to manipulate the controlling factors of BGZ and HFZ. This involves enhancing the thermal conductivity coefficient within the HFZ and augmenting the permeability within the BGZ through some specific reservoir stimulation techniques. With the assistance of R_2, we can systematically conduct various types of gas production enhancement studies.

Table 1
The detailed explanation of the five dynamic dimensionless numbers.

	Formal name	Physical meaning	Indication of magnitude
R_1	Damköhler number	Relative rates of hydrate decomposition and fluid convection.	$R_1 \gg 1$, hydrate decomposition is faster than fluid convection, and convection is the limiting factor. $R_1 \ll 1$, hydrate decomposition is the limiting factor.
R_2	Nusselt number	Ratio of convective and conductive heat transfer.	$R_2 \gg 1$, heat convection is faster than conduction, and heat conduction is the limiting factor. $R_2 \ll 1$, heat convection is the limiting factor.
R_3	Damköhler number	Ratio of hydrate endothermic decomposition and heat convection.	$R_3 \gg 1$, hydrate endothermic decomposition is faster, and convection is the limiting factor. $R_3 \ll 1$, hydrate decomposition is the limiting factor.
R_4	Damköhler number	Ratio of hydrate endothermic decomposition and heat conduction.	Similar to R_3
P_r	Prandtl number	Ratio of the momentum diffusivity and thermal diffusivity.	Similar to R_2

These dynamic dimensionless numbers are capable of dynamically evaluating the intensity relationship of various physical fields at different times and locations, assisting us in identifying the dominant physical processes.

Table 2
Key parameters of simulation model.

Parameter	Value
Sediment density	2650 kg/m^3
Initial temperature	10.325 °C
Initial pressure	12.299 MPa
Porosity	0.3
Intrinsic permeability	10^{-13} m^2
Fracture aperture	0.88 mm
Initial hydrate saturation	0.4
Initial gas saturation	0.0
Production well size	0.1 m × 0.1 m
Injection well size	0.1 m × 0.1 m

7. Conclusions

The physical processes of recovering gas from fractured GHBS are extremely complex. This work proposes a series of dynamic dimensionless numbers to quantify the specific temporal and spatial scale of hydrate reaction, fluid flow, and thermal conduction. Three sets of numerical simulation cases with different injection temperatures, production pressures, and well spacings are conducted to evaluate the multi-physics relations and discuss effective methods to enhance gas production. The analyses combining numerical cases and dynamic dimensionless numbers reaches the following conclusions:

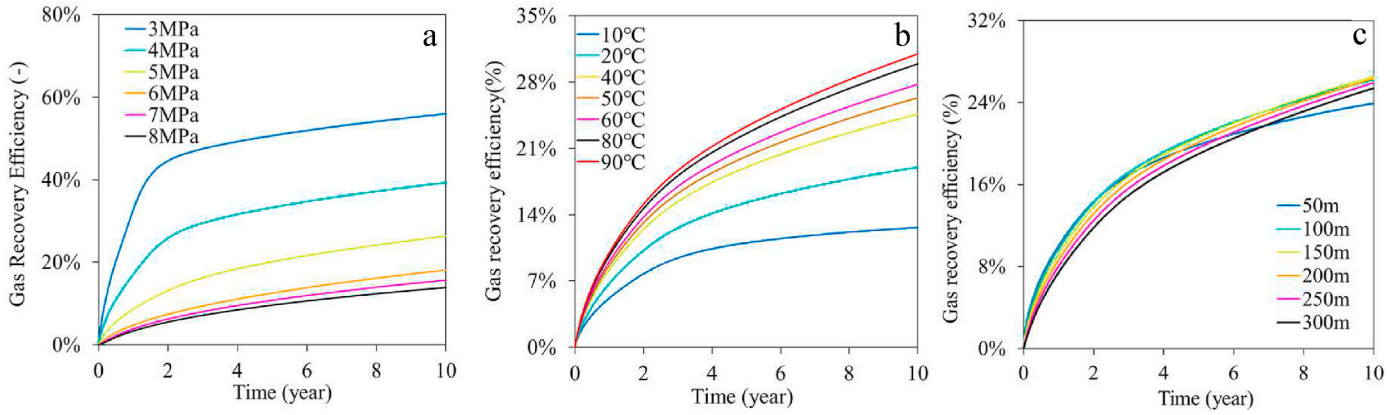

Fig. 18. Gas recovery efficiencies under different production pressure, injection temperature, and well spacing.

(1) During the gas production through heat injection and depressurization, the fractured GHBS can be divided into two parts, namely, HFZ and BGZ. The HFZ extends along the periphery of the fracture.
(2) Changing the injection temperature mainly affects the expansion of HFZ, while adjusting the production pressure mainly affects the saturation evolution in BGZ. Therefore, the increase in gas production resulting from raising the injection temperature is attributed to HFZ. The gas production enhancement by reducing production pressure is mainly attributed to BGZ.
(3) Dynamic dimensionless number analysis shows that thermal conduction is the main controlling factor in HFZ (local scale). Intensifying the thermal conduction process could lead to the expansion of HFZ.
(4) In the short term, thermal conduction is the main limiting factor in BGZ (global scale). In the mediate and long term, fluid flow is the main limiting factor in BGZ, and augmenting fluid flow processes would accelerate the decomposition of hydrates within BGZ at that time. This transition from thermal conduction-limited to fluid flow-limited mode is mainly influenced by injection temperature and production pressure.
(5) If technically feasible, increasing the well spacing is effective to enhance the total gas production without compromising the gas recovery rate.

Glossary

Nomenclature	
C	Mass heat capacity (J/(kg·K))
Da	Damköhler number (−)
E	Specific internal energy (J/kg)
$\boldsymbol{g}$	Gravity vector (0, 0, -9.81 m/s^2)
H	Specific enthalpy (J/kg)
k_0	Intrinsic permeability (m^2)
k_r	Relative permeability (-)
K_b	Klinkenberg factor (-)
λ	Thermal conductivity (W/(mK))
μ	Viscosity of fluid (Pa·s)
L	well spacing (m)
M	Molecule weight (g/mol)
P	Pressure (Pa)
φ	Porosity (−)
q	Mass source and sink (kg/(s·m^3))
R	Dynamic dimensionless number (−)
ρ	Density (kg/m^3)
S	Phase saturation (−)
t	Time (s)
T	Temperature (K)
τ	Characteristic time (−)
v	Velocity of fluid (m/s)
Subscripts	
a	Aqueous phase
g	Gaseous phase
h	Hydrate phase
c	Capillary
s	Sediment matrix
r	Parameters in reference state
0	Original or initial state
f	Fracture
inj	Injection well
prod	Production well
Abbreviations	
NGH	Natural gas hydrate
GHBS	Gas hydrate bearing sediment
HFZ	Hydrate-free zone
BGZ	Background zone
STP	Standard temperature and pressure

CRediT authorship contribution statement

Ming Yang: Conceptualization, Data curation, Formal analysis, Investigation, Methodology, Validation, Visualization, Writing – original draft. **Yuze Wang:** Conceptualization, Data curation, Formal analysis, Funding acquisition, Investigation, Methodology, Project administration, Resources, Supervision, Writing – review & editing. **Hui Wu:** Conceptualization, Data curation, Formal analysis, Investigation, Methodology, Resources, Software, Supervision, Writing – review & editing. **Pengwei Zhang:** Data curation, Formal analysis, Methodology, Visualization. **Xin Ju:** Data curation, Formal analysis, Methodology, Visualization.

Declaration of competing interest

The authors declare that they have no known competing financial interests or personal relationships that could have appeared to influence the work reported in this paper.

Data availability

Data will be made available on request.

Appendix A

The deduction of Damköhler numbers

Firstly, analyzing this problem in the one-dimension condition. At the same time, considering the gas and liquid percolation processes together helps to reduce the complexity.

$$\frac{\partial\left(\rho_a\varphi S_a+\rho_g\varphi S_g\right)}{\partial t}=\frac{\partial}{\partial x}\left(\rho_a v_a+\rho_g v_g\right)+M_h q_h \tag{a1}$$

$$\frac{\partial\left[\varphi\left(\rho_a S_a E_a+\rho_g S_g E_g\right)+(1-\varphi)\rho_s C_s T\right]}{\partial t}=\frac{\partial}{\partial x}\left(\rho_a v_a H_a+\rho_g v_g H_g-\lambda\frac{\partial T}{\partial x}\right)-q_h\Delta H \tag{a2}$$

In order to dimensionlessize these formulas above, the following dimensionless variables need to be introduced

$$\widehat{x}=\frac{x}{L} \tag{a3}$$

$$\widehat{P}=\frac{P_0-P}{P_0-P_b} \tag{a4}$$

$$\widehat{T}=\frac{T-T_0}{T_b-T_0} \tag{a5}$$

$$\widehat{\rho}_a=\frac{\rho_a}{\rho_{a,0}};\widehat{\rho}_g=\frac{\rho_g}{\rho_{g,0}} \tag{a6}$$

$$\widehat{v}_a=\frac{v_a}{v_{a,0}};\widehat{v}_g=\frac{v_g}{v_{g,0}} \tag{a7}$$

$$\widehat{t}=\frac{t}{t_0} \tag{a8}$$

$$\widehat{q}_h=\frac{q_h}{q_{h,0}} \tag{a9}$$

$$\widehat{\lambda}=\frac{\lambda}{\lambda_0} \tag{a10}$$

$$\widehat{H}_a=\frac{H_a}{H_{a0}};\widehat{H}_g=\frac{H_g}{H_{g0}} \tag{a11}$$

$$\Delta\widehat{H}=\frac{\Delta H}{\Delta H_0} \tag{a12}$$

Where L is the characteristic size of the reservoir; the parameters with subscript "0" indicate the initial state value, and that with "b" means the boundary value. $v_{a,0}$ is the initial aqueous velocity, and $v_{g,0}$ is the initial gaseous velocity. t_0 is the initial characteristic time. The effect of gas slip in this process is small and is not the subject of this study, so the Klinkenberg slip factor k_b is ignored. Gravity is also ignored. So, the velocity and characteristic time can be defined as

$$v_{a,0}=\frac{k_{ra,0}k_0}{\mu_{a,0}}\frac{P_0-P_b}{L};v_{g,0}=\frac{k_{rg,0}k_0}{\mu_{g,0}}\frac{P_0-P_b}{L} \tag{a13}$$

$$t_0=\frac{\left(\rho_{a,0}\varphi S_a+\rho_{g,0}\varphi S_g\right)}{M_h q_{h,0}} \tag{a14}$$

Under these treatments, the dimensionless form of equation a1 and equation a2 are

$$\frac{\rho_{a,0}\partial(\widehat{\rho}_a\varphi S_a)+\rho_{g,0}\partial\left(\widehat{\rho}_g\varphi S_g\right)}{\left(\rho_{a,0}\varphi S_a+\rho_{g,0}\varphi S_g\right)\partial\widehat{t}}=\frac{1}{Da^a}\frac{\partial\widehat{\rho}_a\widehat{v}_a}{\partial\widehat{x}}+\frac{1}{Da^g}\frac{\partial\widehat{\rho}_g\widehat{v}_g}{\partial\widehat{x}}+\widehat{q}_h \tag{a15}$$

$$\frac{M_h\partial\left[\varphi\left(\rho_a S_a E_a+\rho_g S_g E_g\right)+(1-\varphi)\rho_s C_s\widehat{T}(T_b-T_0)\right]}{\Delta H\left(\rho_{a,0}\varphi S_a+\rho_{g,0}\varphi S_g\right)\partial\widehat{t}}=\frac{1}{Da^{Ta}}\frac{\partial(\widehat{\rho}_a\widehat{v}_a\widehat{H}_a)}{\partial\widehat{x}}+\frac{1}{Da^{Tg}}\frac{\partial\left(\widehat{\rho}_g\widehat{v}_g\widehat{H}_g\right)}{\partial\widehat{x}}-\frac{1}{Da^T}\frac{\partial}{\partial\widehat{x}}\left(\frac{\widehat{\lambda}\partial\widehat{T}}{\partial\widehat{x}}\right)-\widehat{q}_h\Delta\widehat{H} \tag{a16}$$

Where Da is the Damköhler number, which is used in chemical engineering and chemical kinetics to describe the relative rates of chemical reaction and transport phenomena in a system.

$$Da^a=\frac{M_h q_{h,0}}{\left(\frac{\rho_{a,0}v_{a,0}}{L}\right)}=\frac{M_h q_{h,0}L^2}{\rho_{a,0}k_{ra,0}k_0(P_0-P_b)/\mu_{a,0}} \tag{a17}$$

$$Da^{g}=\frac{M_h q_{h,0}}{\left(\frac{\rho_{g,0}v_{g,0}}{L}\right)}=\frac{M_h q_{h,0}L^2}{\rho_{g,0}k_{rg,0}k_0(P_0-P_b)/\mu_{g,0}} \tag{a18}$$

$$Da^{Ta}=\frac{q_{h,0}\Delta H_0 L}{\rho_{a,0}H_{a,0}v_{a,0}}=\frac{q_{h,0}\Delta H_0 L^2}{\rho_{a,0}H_{a,0}k_{ra,0}k_0(P_0-P_b)/\mu_{a,0}} \tag{a19}$$

$$Da^{Tg}=\frac{q_{h,0}\Delta H_0 L}{\rho_{g,0}H_{g,0}v_{g,0}}=\frac{q_{h,0}\Delta H_0 L^2}{\rho_{g,0}H_{g,0}k_{r,g0}k_0(P_0-P_b)/\mu_{g,0}} \tag{a20}$$

$$Da^{T}=\frac{q_{h,0}\Delta H_0 L^2}{\lambda_0(T_b-T_0)} \tag{a21}$$

Da^{a} and Da^{g} are the Damköhler number of aqueous phase flow and gaseous phase flow respectively, the physical meaning of which are the relative strength of the chemical reaction in relation to the convective flow in the corresponding phase of fluid; Da^{Ta} and Da^{Tg} are the Damköhler number of aqueous and gaseous phase thermal flow respectively, with the physical meaning of the relative strength of the thermal process of a chemical reaction in relation to convective heat transfer. Da^{T} is the Damköhler number of the heat conduction process, and the physical meaning is the relative strength of the chemical reaction heat process and heat conduction. Da^{Ta} and Da^{Tg} are the results of superimposing energy transport on Da^{a} and Da^{g} respectively, and there is an overlap in their physical meanings. As a result, it is feasible to select only Da^{a} and Da^{g} for further research. Additionally, M_h is the molecular weight of methane hydrate, which is 160 g/mol in this work.

References

[1] Sloan ED. Fundamental principles and applications of natural gas hydrates. Nature 2003;426(6964):353–9. https://doi.org/10.1038/nature02135.

[2] Milkov AV. Global estimates of hydrate-bound gas in marine sediments: how much is really out there? Earth Sci Rev 2004;66(3–4):183–97. https://doi.org/10.1016/j.earscirev.2003.11.002.

[3] Ye JL, Qin XW, Xie WW, Lu HL, Ma BJ, Qiu HJ, et al. The second natural gas hydrate production test in the South China Sea. China Geology 2020;3(2):197–209. https://doi.org/10.31035/cg2020043.

[4] Lee J, Park S, Sung W. An experimental study on the productivity of dissociated gas from gas hydrate by depressurization scheme. Energy Convers Manag 2010;51(12):2510–5. https://doi.org/10.1016/j.enconman.2010.05.015.

[5] Konno Y, Masuda Y, Hariguchi Y, Kurihara M, Ouchi H. Key factors for depressurization-induced gas production from oceanic methane hydrates. Energy Fuel 2010;24(3):1736–44. https://doi.org/10.1016/j.apenergy.2020.115393.

[6] Myshakin EM, Gaddipati M, Rose K, Anderson BJ. Numerical simulations of depressurization-induced gas production from gas hydrate reservoirs at the Walker Ridge 313 site, northern Gulf of Mexico. Mar Petrol Geol 2012;34(1):169–85. https://doi.org/10.1016/j.marpetgeo.2011.09.001.

[7] Cheng F, Sun X, Li Y, Ju X, Yang Y, Liu X, et al. Numerical analysis of coupled thermal-hydro-chemo-mechanical (THCM) behavior to joint production of marine gas hydrate and shallow gas. Energy 2023;281:128224. https://doi.org/10.1016/j.energy.2023.128224.

[8] Moridis GJ, Reagan MT, Boyle KL, Zhang KN. Evaluation of the gas production potential of some particularly challenging types of oceanic hydrate deposits. Transport Porous Media 2011;90(1):269–99. https://doi.org/10.1007/s11242-011-9762-5.

[9] Li XS, Wan LH, Li G, Li QP, Chen ZY, Yan KF. Experimental investigation into the production behavior of methane hydrate in porous sediment with hot brine stimulation. Ind Eng Chem Res 2008;47(23):9696–702. https://doi.org/10.1021/ie8009582.

[10] Wu S, Zhou X, Lu J, Liang D, Li D. Experimental study on CH4 hydrate dissociation by the injection of hot water, brine, and ionic liquids. J Mar Sci Eng 2023;11(4):713. https://doi.org/10.3390/jmse11040713.

[11] Kurihara M, Sato A, Ouchi H, Narita H, Masuda Y, Saeki T, et al. Prediction of gas productivity from Eastern Nankai Trough methane-hydrate reservoirs. SPE Reservoir Eval Eng 2009;12(3):477–99. https://doi.org/10.2118/125481-PA.

[12] Zeng H, Zhang Y, Zhang L, Chen Z, Li X. Study on hydrate production behaviors by depressurization combined with brine injection in the excess-water hydrate reservoir. Entropy 2022;24(6):765. https://doi.org/10.3390/e24060765.

[13] Ma Y, Zhong X, Li X, Nie S, Li Q, Tu G, et al. Numerical simulation of gas extraction from marine hydrate sediments using sodium chloride injection. Fuel 2023;342:127910. https://doi.org/10.1016/j.fuel.2023.127910.

[14] Zhang Y, Cui M, Li D, Xin G. Microscopic insights and optimization of the CH4–CO2 replacement in natural gas hydrates. ACS Omega 2022;7(50):47239–50. https://doi.org/10.1021/acsomega.2c06502.

[15] Wang X, Sun Y, Li B, Zhang G, Guo W, Li S, et al. Reservoir stimulation of marine natural gas hydrate-a review. Energy 2023;263(15):126120. https://doi.org/10.1016/j.energy.2022.126120.

[16] Sun X, Luo TT, Wang L, Wang HJ, Song YC, Li YH. Numerical simulation of gas recovery from a low-permeability hydrate reservoir by depressurization. Appl Energy 2019;250:7–18. https://doi.org/10.1016/j.apenergy.2019.05.035.

[17] Anderson B, Hancock S, Wilson S, Enger C, Collett T, Boswell R, et al. Formation pressure testing at the Mount Elbert gas hydrate stratigraphic test well, Alaska north slope: operational summary, history matching, and interpretations. Mar Petrol Geol 2011;28(2):478–92. https://doi.org/10.1016/j.marpetgeo.2010.02.012.

[18] Dai S, Kim J, Xu Y, Waite WF, Jang J, Yoneda J, et al. Permeability anisotropy and relative permeability in sediments from the national gas hydrate program expedition 02, offshore India. Mar Petrol Geol 2019;108:705–13. https://doi.org/10.1016/j.marpetgeo.2018.08.016.

[19] Jang J, Waite WF, Stern LA, Lee JY. Diatom influence on the production characteristics of hydrate-bearing sediments: examples from Ulleung Basin, offshore South Korea. Mar Petrol Geol 2022;144:105834. https://doi.org/10.1016/j.marpetgeo.2022.105834.

[20] Liu X, Zhang W, Qu Z, Guo T, Sun Y, Rabiei M, et al. Feasibility evaluation of hydraulic fracturing in hydrate-bearing sediments based on analytic hierarchy process-entropy method (AHP-EM). J Nat Gas Sci Eng 2020;81:103434. https://doi.org/10.1016/j.jngse.2020.103434.

[21] Sun Y, Li S, Lu C, Liu S, Chen W, Li X. The characteristics and its implications of hydraulic fracturing in hydrate-bearing clayey silt. J Nat Gas Sci Eng 2021;95:104189. https://doi.org/10.1016/j.jngse.2021.104189.

[22] Chen C, Yang L, Jia R, Sun Y, Guo W, Chen Y, et al. Simulation study on the effect of fracturing technology on the production efficiency of natural gas hydrate. Energies 2017;10(8):1241. https://doi.org/10.3390/en10081241.

[23] Feng Y, Chen L, Suzuki A, Kogawa T, Okajima J, Komiya A, et al. Enhancement of gas production from methane hydrate reservoirs by the combination of hydraulic fracturing and depressurization method. Energy Convers Manag 2019;184:194–204. https://doi.org/10.1016/j.enconman.2019.01.050.

[24] Sun J, Ning F, Liu T, Liu C, Chen Q, Li Y, et al. Gas production from a silty hydrate reservoir in the South China Sea using hydraulic fracturing: a numerical simulation. Energy Sci Eng 2019;7(4):1106–22. https://doi.org/10.1002/ese3.353.

[25] Guo W, Zhang P, Wang Y, Jia R, Li B. Evolution on the gas production from low permeability gas hydrate reservoirs by depressurization combined with reservoir stimulation. Energy Fuel 2020;34(12):15819–28. https://doi.org/10.1021/acs.energyfuels.0c02382.

[26] Han D, Wang Z, Xu A. Gas production from fractured hydrate reservoirs: numerical modeling and evaluation. Energy Technol 2021;9(10):2100518. https://doi.org/10.1002/ente.202100518.

[27] Shang S, Gu L, Lu H. The effects of the length and conductivity of artificial fracture on gas production from a Class 3 hydrate reservoir. Energies 2021;14(22):7513. https://doi.org/10.3390/en14227513.

[28] Li S, Wu D, Wang X, Hao Y. Enhanced gas production from marine hydrate reservoirs by hydraulic fracturing assisted with sealing burdens. Energy 2021;232(1):120889. https://doi.org/10.1016/j.energy.2021.120889.

[29] Ning F, Chen Q, Sun J, Wu X, Cui G, Mao P, et al. Enhanced gas production of silty clay hydrate reservoirs using multilateral wells and reservoir reformation techniques: numerical simulations. Energy 2022;254(1):124220. https://doi.org/10.1016/j.energy.2022.124220.

[30] Xu T, Zhang Z, Li S, Li X, Lu C. Numerical evaluation of gas hydrate production performance of the depressurization and backfilling with an in situ supplemental heat method. ACS Omega 2021;6(18):12274–86. https://doi.org/10.1021/acsomega.1c01143.

[31] Ye H, Wu X, Li D, Jiang Y, Gong B. A novel thermal stimulation approach for natural gas hydrate exploitation — the application of the self-entry energy compensation device in the Shenhu sea. J Nat Gas Sci Eng 2022;105:104723. https://doi.org/10.1016/j.jngse.2022.104723.

[32] Li XY, Tian YY, Zhang X, Song G, Zhao M, Liang JQ, et al. Numerical simulation study on the effect of horizontal well reservoir stimulation for gas hydrate production. Acta Geol Sin-Engl Ed. 2022;96(2):701–12. https://doi.org/10.1111/1755-6724.14930.

[33] Feng JC, Li B, Li XS, Wang Y. Effects of depressurizing rate on methane hydrate dissociation within large-scale experimental simulator. Appl Energy 2021;304:117750. https://doi.org/10.1016/j.apenergy.2021.117750.
[34] Ju X, Liu F, Fu PC, White MD, Settgast RR, Morris JP. Gas production from hot water circulation through hydraulic fractures in methane hydrate-bearing sediments: THC-coupled simulation of production mechanisms. Energy Fuel 2020;34(4):4448–65. https://doi.org/10.1021/acs.energyfuels.0c00241.
[35] Yu T, Guan G, Wang D, Song Y, Abudula A. Gas production enhancement from a multilayered hydrate reservoir in the South China Sea by hydraulic fracturing. Energy Fuel 2021;35(15):12104–18. https://doi.org/10.1021/acs.energyfuels.1c01785.
[36] Oluwunmi P, Pecher I, Archer R, Reagan M, Moridis G. The response of gas hydrates to tectonic uplift. Transport Porous Media 2022;144(3):739–58. https://doi.org/10.1007/s11242-022-01837-w.
[37] Li XY, Feng JC, Li XS, Wang Y, Hu HQ. Experimental study of methane hydrate formation and decomposition in the porous medium with different thermal conductivities and grain sizes. Appl Energy 2022;305:117852. https://doi.org/10.1016/j.apenergy.2021.117852.
[38] Teng Y, Zhang D. Comprehensive study and comparison of equilibrium and kinetic models in simulation of hydrate reaction in porous media. J Comput Phys 2020;404(1):109094. https://doi.org/10.1016/j.jcp.2019.109094.
[39] Liu Y, Chen Y, Bai Y, Li S. Similarity theory for the physical simulation of natural gas hydrate reservoir development. Min Sci Technol 2010;20(5):782–8. https://doi.org/10.1016/S1674-5264(09)60281-7.
[40] Sun X, Nanchary N, Mohanty KK. 1-D modeling of hydrate depressurization in porous media. Transport Porous Media 2005;58(3):315–38. https://doi.org/10.1007/s11242-004-1410-x.
[41] Zhang ZB, Xu T, Li SD, Li X, Briceño Montilla MJ, Lu C. Comprehensive effects of heat and flow on the methane hydrate dissociation in porous media. Energy 2023;265(15):126425. https://doi.org/10.1016/j.energy.2022.126425.
[42] Zhang PW, Liu BG, Hu LM, Meegoda JN. Coupled multiphase flow and pore compression computational model for extraction of offshore gas hydrates. Comput Geotech 2022;145:104671. https://doi.org/10.1016/j.compgeo.2022.104671.
[43] Moridis GJ. User's manual for the hydrate v1. 5 option of TOUGH+ v1. 5: a code for the simulation of system behavior in hydrate-bearing geologic media. Berkeley, CA (United States): Lawrence Berkeley National Lab.(LBNL); 2014. https://www.osti.gov/biblio/1165986/.
[44] van Genuchten MT. A closed-form equation for predicting the hydraulic conductivity of unsaturated soils. Soil Sci Soc Am J 1980;44(5):892–8. https://doi.org/10.2136/sssaj1980.03615995004400050002x.
[45] Dai S, Seol Y. Water permeability in hydrate-bearing sediments: a pore-scale study. Geophys Res Lett 2014;41(12):4176–84. https://doi.org/10.1002/2014GL060535.
[46] Stone HL. Probability model for estimating 3-phase relative permeability. J Petrol Technol 1970;22:214–8. https://doi.org/10.2118/2116-PA.
[47] Parker JC, Lenhard RJ. A model for hysteretic constitutive relations governing multiphase flow: 1. Saturation-pressure relations. Water Resour Res 1987;23(12):2187–96. https://doi.org/10.1029/WR023i012p02197.
[48] Witherspoon PA, Wang JSY, Iwai K, Gale JE. Validity of Cubic Law for fluid flow in a deformable rock fracture. Water Resour Res 1980;16(6):1016–24. https://doi.org/10.1029/WR016i006p01016.
[49] Zhang H, Yang S, Wu N, Su X, Holland M, Schultheiss P, et al. Successful and surprising results for China's first gas hydrate drilling expedition. Fire in the Ice: Methane Hydrate Newsletter 2007;7(3):6–9.
[50] Li JF, Ye JL, Qin XW, Qiu HJ, Wu NY, Lu HL, et al. The first offshore natural gas hydrate production test in South China Sea. China Geology 2018;1(2):202–9. https://doi.org/10.31035/cg2018003.
[51] Settgast RR, Fu P, Walsh SDC, White JA, Annavarapu C, Ryerson FJ. A fully coupled method for massively parallel simulation of hydraulically driven fractures in 3-dimensions. Int J Numer Anal Methods GeoMech 2017;41(5):627–53. https://doi.org/10.1002/nag.2557.
[52] White MD, Kneafsey TJ, Seol Y, Waite WF, Uchida S, Lin JS, et al. An international code comparison study on coupled thermal, hydrologic and geomechanical processes of natural gas hydrate-bearing sediments. Mar Petrol Geol 2020;120:55. https://doi.org/10.1016/j.marpetgeo.2020.104566.
[53] Wang L, Wu S, Li Q, Wang D, Fu S. Architecture and development of a multi-stage baiyun submarine slide complex in the pearl river canyon, northern South China sea. Geo Mar Lett 2014;34(4):327–43. https://doi.org/10.1007/s00367-014-0372-4.
[54] Song Y, Cheng C, Zhao J, Zhu Z, Liu W, Yang M, et al. Evaluation of gas production from methane hydrates using depressurization, thermal stimulation and combined methods. Appl Energy 2015;145:265–77. https://doi.org/10.1016/j.apenergy.2015.02.040.
[55] Sun S, Gu L, Tian W, Lin H, Yang Z. Percolation characteristics of pore fluid during hydrate depressurization dissociation from multi-phase multi-field coupling analysis. Energy 2023;281:128296. https://doi.org/10.1016/j.energy.2023.128296.